Impact Velocity-Dependent Bonding Mechanisms in Metal Cold Spray

C.D. Reddy[1] *, Zhi-Qian Zhang[1] §, S. Msolli[2], Junyan Guo[1], N. Sridhar[1]

[1] Institute of High Performance Computing, A*STAR Research Entities,

1 Fusionopolis Way, #16-16 Connexis, Singapore 138632

[2] ICB UMR 6303, CNRS, Université Bourgogne Franche-Comté, UTBM, F-90010 Belfort, France

*** Contact email: reddy@ihpc.a-star.edu.sg, § zhangz@ihpc.a-star.edu.sg**

Abstract

In this paper, we probe the bonding mechanisms for an impacting particle on a substrate, as in the cold spray process, over a range of impact velocities using molecular dynamics simulations. For the model copper/copper system, we find that grain boundary-like amorphous phase interlocking and metallurgical bonding are dominant at low and medium impact velocities, respectively, while metallurgical bonding and mechanical interlocking are dominant at high impact velocities. In particular, features including substrate crater depth, particle flattening ratio, and jetting area are tracked with varying impact velocities to further enhance our understanding of the underlying bonding mechanisms and the grain refinement in and around the interface. Because our findings are based only on small particle simulations allowable in MD, size effects can preclude extrapolating the results to physical micron-sized particles used in actual cold spray.

Keywords: Interface bonding, jetting, flattening, interlocking, nanotwins, cold spray

1. Introduction

High-velocity impact-induced bonding between metals as in the cold spray process is enticing due to the high deposition efficiency and thus in a wide range of industrial applications such as for metallic coatings on surfaces, repair of components, additive manufacturing, and forming of bulk materials [1-3]. A variety of impact-induced bonding mechanisms between the particle and substrate have been proposed including adiabatic shear instability [4-6], hydrodynamic plasticity [7], local melting [8, 9], interface diffusion [10], amorphization of the interface [11], metallurgical bonding [12-14], and mechanical interlocking [12, 15, 16]. These proposed mechanisms are based on the analysis of experimental data with analytical models. There are, however, few direct experimental observations of the bonding mechanism due to the structural complexity, and also because bonding occurs in a short time (sub-nanosecond) and length (nanometer) scales making experimental access very difficult [7, 17].

In principle, two atomically clean surfaces brought together in the atomic spatial range can bond with each other. In cold spray, the high impact velocity of the particle provides the necessary condition to bring the surfaces atomically into close contact for bonding [18]. At the critical impact velocity, a threshold velocity when a jet of material starts ejecting from the particle-substrate interface [19, 20], bonding has been attributed to adiabatic shear instability (ASI) [5, 6, 21]. However, there is no experimental evidence supporting ASI as the main cause for bonding [7]. Recently, there has also been much debate in the literature on whether hydrodynamic plasticity or ASI is the cause for bonding [7, 18, 22]. To probe atomic-level bonding mechanisms, molecular dynamics (MD) simulations have been reported for a small particle containing a few thousand atoms [23-27]. Although MD and quasi-coarse-grained models [28-30] show jetting phenomena for high impact velocities (1000 m/s and beyond), there are no reported MD results in and around the critical velocity except for our previous work [12]. At the critical impact velocity, the bonding

mechanisms were elucidated qualitatively. We pointed out that the nature of the bonding is a combination of grain boundary-like amorphous interface bonding, metallurgical bonding, and mechanical interlocking [12]. In the current work, we illustrate microstructural changes with impact velocity, studies that are not accessible from experimental and FEM studies. During cold spray experiments, the particles impacting the surface obey a velocity distribution, and hence, the resultant local deformed structure is very complex. Understanding the deformation of the particle and the coating at different velocities is vital to understanding the resultant microstructure and the bonding mechanisms. Hence, with MD simulations, we probe the impact process for a range of impact velocities and track features including particle flattening ratio, crater depth, local melting behavior, mechanical interlocking, metallurgical grain formation, and their role on bonding.

The extrapolation of MD results from nanometer-sized particles to the micron-sized particle is complicated since particle size has a role in the localized melting characteristics and the deformation behavior of the particle and substrate. However, modeling a micron-size particle with MD is impractical due to the prohibitively expensive computational cost. The particle (nanometer size) considered in this study is much smaller (1000X smaller) and hence the findings need to be considered with caution while extending the results to micron size particles used in cold spray experiments.

2. Simulation Method

We consider a spherical single crystal copper particle with a diameter D of 200 Å and a cuboid single crystal copper substrate of size $8D$ x $8D$ x $4D$ with 170,755,200 atoms. The classical molecular dynamic package LAMMPS (Large-scale Atomic/Molecular Massively Parallel Simulator) [31] with EAM (Embedded Atom Method) potential [32, 33] is used for the copper/copper system. Further details of the simulation method and the EAM potential validation

are presented in the supplementary material and our previous work [12]. The system is periodic the direction perpendicular to the particle impact direction (x- and y- directions in Fig. 1). The top surface of the substrate (z-direction) is free of any constraints. At the substrate bottom, a few atomic layers are constrained to support the system mechanically. To mimic room temperature simulations, the particle and the substrate are equilibrated at 300 K, with canonical ensemble (NVT) settings, before the particle impacts with the designated velocity. We only consider a pure single crystal copper/copper system without a native oxide layer, to avoid additional complexity. The open visualization tool (OVITO) is used to capture the atomic configurations during the simulation process [34].

3. Results and Discussion

When a spherical particle impacts the substrate with high velocity, a permanent crater is created on the substrate, and the crater size reflects the extent of substrate deformation (Fig. 1). At the same time, the particle flattens due to the impact. The flattening ratio can be defined as the compressive strain ε ($\varepsilon = 1-h/D$) in the particle, where h is the height of the particle after deformation and D is the initial diameter of the particle. The flattening ratio depends on the impact velocity of the particle and the material properties of the particle and substrate. The variations in equilibrium crater depth d and equilibrium flattening ratio ε with impact velocity (Fig. 2a), can be broadly divided into three regimes as follow:

- Regime I: Below the critical impact velocity (in the range of 200 to 450 m/s), both d and ε monotonically increase and with the particle deforming into more of an oblate spheroid. At the interface, the material melts locally, and gradually the melt volume increases as impact velocity increases, forming a thin amorphous layer between the particle and substrate. To the best of our knowledge, experimental observations are not available in the literature for

this regime to compare with our results directly. In this low-velocity regime, MD simulations indicate the particle will be poorly bonded to the substrate due to the intrinsic weakness of the grain boundary-like amorphous interface. (In actual setting, the poor interface bonding, or no bonding, is likely due to the oxide layer covering the particle and substrate surfaces not breaking and thus the continuous amorphous interface not getting established). Coincidentally, finite element simulations [5, 35, 36] also capture the monotonic increase in particle flattening ratio for this velocity regime (Supplementary material Fig. S2).

- Regime II: For velocity in the 450 m/s to 550 m/s range, sandwiching the critical impact velocity of around 500 m/s [20, 37], d saturates and the initiation of material jetting leads to enhanced bonding (discussed later in this paper). Due to jetting, the flattening of the particle into an oblate spheroid shape is not strictly followed and there is nominal plateauing of the ε in this regime.
- Regime III: For impact velocity beyond 550 m/s, d sharply increases with velocity because of the large melt volume generated in the substrate, whereas ε plateaus after a small increase and the particle is confined to the crater with some amount of jet ejected along with the interface. A similar phenomenon of particle confinement to the crater has also been observed in experiments for a single particle with a high impact velocity [17].

We also trace the time evolution of d and ε for the velocity of 500 m/s, as shown in Fig. 2(b). The crater depth increases due to the deformation of the substrate by localized melting, plastic deformation, and jetting from the interface edge by the penetrating particle. Because of elastic recovery in both particle and substrate, d and ε partially decrease (after 20 ps) from their peak compression values. As the system cools down, they plateau and attain a constant value.

During the impact of the high-velocity particle, the particle kinetic energy is partially transformed to heat at the interface region in the first few picoseconds and as a result the material around the interface gradually melts. In the next few picoseconds, more thermal energy transfers from the interface to the surroundings, and bonding occurs at the interface during the solidification process. The maximum total volume of molten material, from both particle and substrate, is reached at around 6 ps after impact and the corresponding snapshots are captured in Fig. 3. At an impact velocity of 300 m/s, the molten material (red zone) is mostly confined around the center of the interface. At 400 m/s, the melt volume is more spread out across the interface between the particle and substrate. At 500 m/s, the melt volume from both particle and substrate increases further and shows signs of jetting at the edge of the interface (Fig. 3c). At 600 m/s, nominally beyond the critical impact velocity, a considerably large material melts and starts to squeeze out from the interface region (Fig 3d). The material jetting initiates mechanical interlocking, as discussed in the latter part of this paper.

Figure 4a quantifies the evolution of the melt portion for both the particle and substrate. This is presented for a range of impact velocities. The atoms exceeding the melting temperature (1360 K for bulk copper) are normalized by the total number of particle atoms. In the initial stage, the number of atoms at any instant exceeding the melt temperature is larger for the substrate than for the particle. However, at a later stage, the substrate atoms cool down faster than the particle atoms (except for the 600 m/s case). Since the substrate is hooked to a heat sink and with no heat loss on the particle side, atoms on the substrate side of the interface region cool down faster than the atoms on the particle side of the interface. For the 600m/s case, the substrate atoms in the jet area (outer rim of the interface) cool relatively slower than the particle atoms.

Upon particle impact, the melt volume is pushed towards the interface edge leading to the formation of a rim-like pileup between the particle and substrate schematically illustrated in Fig. 1. After considerable time, allowing for the system to cool down, the atomic structure of the particle and substrate are captured for 200 m/s and 300 m/s as shown in Fig. 5 and for higher velocities shown in Figs. 6 and 7. The approximated interface (shown as a dotted line) illustrates the demarcation between the particle and substrate atoms. The majority of atoms in the system are in the FCC structure (represented as green atoms). The thin red lines between the FCC crystals indicate deformation-induced nano-twins that are in the HCP structure. These nano-twins accommodate large strain between different parts of the microstructure and increase the strength of the material [40]. The white atoms represent the amorphous structure located at the interface, between the grains as well as in the edges of the nano-twin. There are small blue regions in the amorphous zone, representing the BCC structure. Since deformation in the particle and substrate initiates along atomically weak planes upon impact, asymmetric deformations in the particle and substrate are produced. Such features cannot be captured using finite element simulations due to the uniform homogenized material properties considered [7, 36, 41] in those calculations.

At impact velocities of 200 m/s and 300 m/s, the particle creates a shallow crater on the substrate and produces a thin melted region along with the interface during impact. At this interface, the atoms form a thin amorphous (grain boundary-like) region as shown in Fig. 5. Even though size effects preclude extending the MD results to physical microscale particles, a similar thin amorphous structure (~layer of 3 nm) has been observed between the particle and substrate using TEM [42]. This thin amorphous interface region is expected to result in relatively weak strength compared to the crystalline metallurgical bond formed at higher impact velocities. At both velocities of 200 m/s and 300 m/s, sub-grains are formed in the substrate just below the center of

the interface. For 300 m/s, smaller grains (shear-induced regions) are formed in the substrate material near one edge of the interface.

Figure 6 shows the equilibrium structure of the system for an impact velocity of 400 m/s to 600 m/s. At 400 m/s velocity, there is considerable melt volume around the interface squeezed out from the interface edge. New edge metallurgical grains with stacking fault regions (nano twins) are formed with the material sheared off from the interface and this edge grain is referred to as Edge Metallurgical Grain (EMG). The major portion of EMG is comprised of material originating from the substrate, and the interface passes through the upper portion of these grains as shown by the dashed line in Fig. 6.

At the critical impact velocity of 500 m/s, a large melt volume comprising of both particle and substrate material intermix and plastically flow out as a jet along the interface edge. After jetting, the remaining melt volume at the edge of the interface results in a large EMG as shown in Fig. 6. The material jet from the interface forms a thin curved hook-like strip on the EMG, interlocking the particle and substrate grains along the outer periphery of the interface. This thin strip can lead to further folding into a roll-up form [15] from subsequent impacting particles deposited during the process, enhancing the interface bonding strength. This phenomenon is the primary cause for bonding from mechanical interlocking. At the center part of the compressive region (below the bottom of the particle), the trapped melt volume forms a large grain, labeled as a metallurgical grain (MG). This grain resulting from inter-diffusion contains atoms from both particle and substrate. The interface consists of three parts including mechanical interlocking at the periphery, metallurgical bonding (MG and EMG regions), and a grain-boundary-like amorphous region between MG and EMG at the interior part of the interface. Thus, the bonding mechanisms are a combination of grain boundary-like interlocking, metallurgical bonding, and mechanical

interlocking. Further details of the bonding mechanisms at the critical velocity are presented in our earlier work [12].

At the impact velocity of 600 m/s, the high-impact energy creates a deep crater in the substrate, flattening the particle and with the entire particle embedded inside the crater. Due to the large melt volume generated at the interface, a wide jet emerges and this results in a thin strip covering the EMG (cross-sectional view shown in Fig. 6 and only particle shown in supplementary information Fig. S3), enhancing further the mechanical interlocking at the edges of the interface. At the center, metallurgically bonded grains are seamlessly connected to the substrate, just as in the 500 m/s case. The total occupied volume of the EMG is also greater than that at lower velocities. Beyond the critical velocity (as in regime III), the particle penetrates even deeper into the substrate resulting in potentially stronger mechanical interlocking and thus increased interface bonding strength between the particle and substrate than in regime II [17].

We show in Fig. 7, the atomic structure of the particle peering into the interface from the bottom (in addition to the cross-sectional views shown in Fig. 6) for impact velocities of 500 m/s and 600 m/s. The supplementary material Fig. S4 shows that for lower velocities (200 m/s to 400 m/s). The material plastically deforms at the contact surface forming a grain-boundary-like amorphous layer (white) with the interface mostly covered with this layer but with scattered shallow green patches (metallurgically bonded regions). As the velocity increases, atoms from the trapped molten material at the interface region dynamically crystallize and merge with the substrate atoms and as a result, the green patches increase and the white area gradually reduces. At impact velocities of 500 m/s and 600 m/s (Fig. 6), it is clear that part of the particle volume is seamlessly connected to the substrate with the depth of the green patch increasing. In Fig. 7, the region outside the black circle represents the ejected material from the particle as a jet from the interface. At an impact velocity of 500 m/s, the melt material ejecting from the interface region leads to the formation of

mechanical interlocks (anchoring) with the substrate melt material. The plastically deformed material near the edges forms edge metallurgical grains with nano-twins (large stacking fault regions) visible inside the black circle. At 600 m/s, there is a wider jetting region around the particle (Fig. S3) indicating even more extensive mechanical interlocking when compared to the 500 m/s case. In the critical velocity regime, current simulations are in good agreement with single particle experiments [17] showing jetting initiating around the particle (Fig. 7) and also a wider jetting area with increasing velocity.

A monotonic increase in particle flattening with the increase of the impact velocity has been reported using finite element simulations [35, 36]. However, current MD simulations show that particle flattening does not follow a monotonic increase. Instead, it varies based on the velocity regime as in single particle experiments [17]. We also note that since cold spray is a high impact velocity driven process, the initial particle crystallographic orientation with respect to the substrate does not influence the bonding mechanism but can have some influence on the final deformed shape of the particle and the final microstructure (Fig. S5) [28].

The current simulations improve our understanding of the bonding mechanisms in different regimes, both qualitative and quantitatively. The kinetic energy of the impacting particle is the driving force for melting around the interface (temperature profile as shown in Fig. 3). The interface surface area provides a quantitative description of the type of bonding between the particle and substrate, as shown in Fig. 8. In this figure, the Y-axis represents the interface surface area normalized with the interface surface area for the impact velocity of 650 m/s. For comparison, the interface area for an impact velocity of 650 m/s is almost 3 times that at 300 m/s. The relative coverage of grain boundary-like amorphous interface, metallurgical bonding, and mechanical interlocking at each velocity provides an understanding of the qualitative bonding strength. The change in interface coverage with the three bonding types can also be distinguished into three

regimes, just as for the crater depth and flattening ratio shown in Fig. 2a. At impact velocity below 300 m/s, the low kinetic energy of the particle causes less surface melting around the interface leading to the formation of grain boundary-like interface bonding (Fig. 5). As velocity increases in regime I, the melt volume increases (Fig. 4) due to moderate particle kinetic energy, and the molten material is pushed to the interface edge leading to the formation of EMG (edge metallurgical grains) and a thin grain boundary-like amorphous phase at the inner part of the interface (marked as a yellow loop in Fig. 6). The area of metallurgical bonding increases with impact velocity whereas the grain boundary-like area is almost the same (relative grain boundary-like surface decrease). In this regime I, both grain boundary-like interface and metallurgical bonding are the main bonding mechanisms.

In the critical velocity regime II, the higher impact energy increases produce larger melt volume (Fig. 4) at the interface region, and significant material plastically flows towards the edge of the interface leading to partial jetting and formation of moderate EMGs. At the center of the interface, the remaining molten material crystallized into a metallurgical grain. In this regime, metallurgical bonding and mechanical interlocking are dominant mechanisms for bonding and the grain boundary-like amorphous phase effect is minimum. We also note that at the critical velocity of impact, material jetting is seen in experiments and finite element simulations [5, 6, 21]. However, MD simulations have not reported observation of jetting at the critical velocity regime except for our previous work [12].

In the higher impact velocity regime III, increased kinetic energy leads to significantly more molten material and with that flowing towards the edge. Around 40% of that flowing material form EMG and MG grains, 20% material into a grain boundary-like amorphous structure, and the remaining ejecting as a jet. As the velocity increases, the increased jetting leads to a larger surface area of

mechanical interlocking along the outer periphery of the interface. In this high-velocity regime, the bonding strength will be stronger than it is in regime II due to the enhancement from mechanical interlocking as well as metallurgical bonding. At the impact velocity of 650 m/s, metallurgical and mechanical bonding covers 82% of the particle/substrate interface, and the remaining 18% is covered by the grain-boundary-like (amorphous) interface.

Table 1 shows the summary of bonding mechanisms and the dominant bonding mechanisms are highlighted in bold letters. We highlight numerous studies, containing both experimental findings and finite element analysis [7, 18, 22], show the impact of a particle on a substrate leading to material jetting at the critical velocity. However, the bonding mechanism between the particle and substrate was not clearly understood. This study addresses that by shedding light on a fundamental understanding of the bonding mechanisms at different velocity regimes and thus enable the development of guidelines for process improvement of the cold spray additive manufacturing process.

4. Conclusions

We presented molecular dynamics simulation results showing impact velocity-dependent bonding mechanisms. Since interface bonding occurs at the sub-nanosecond time and nanometer length scales, variations of the flattening ratio, crater depth, and jetting were studied to get a critical understanding of the underlying bonding mechanisms over a wide range of velocities. Based on their characteristics, three regimes were identified. In the low-velocity regime I, lower melt volume leads to insufficient material available to form new grains at the interface and the primary bonding is from a disordered interface that is grain boundary-like. In the intermediate velocity regime II, the larger melt volume causes edge and middle metallurgical grains formed, leading to

metallurgical bonding along with the interface. In the higher velocity regime III, material jetting from the interface region leads to mechanical interlocking around the edge metallurgical grains with both metallurgical bonding and mechanical interlocking as the primary bonding mechanisms. We find that high-velocity impact can lead to localized melting at the interface with different melt volume scaling behavior for the particle and substrate. The subsequent grain formation provides for a more detailed understanding of the bonding mechanisms in the cold spray process.

Acknowledgment

We acknowledge support for this work by A*STAR, Singapore with funding from grant No: A1894a0032 and grant No: A18B1b0061. This work was carried out on high performance computing facilities of A*STAR Computational Resource Centre (A*CRC).

References:

[1] S.M. Hassani-Gangaraj, A. Moridi, M. Guagliano, Critical review of corrosion protection by cold spray coatings, Surf. Eng. 31 (2015) 803–815

[2] X. Wang, F. Feng, M.A. Klecka, M.D. Mordasky, J.K. Garofano, T. El-Wardany, A. Nardi, V.K. Champagne, Characterization and modeling of the bonding process in cold spray additive manufacturing, Addit. Manuf. 8 (2015) 149–162

[3] N.H. Tariq, L. Gyansah, J.Q. Wang, X. Qiu, B. Feng, M.T. Siddique, T.Y. Xiong, Cold spray additive manufacturing: a viable strategy to fabricate thick B4C/Al composite coatings for neutron shielding applications, Surf. Coat. Technol. 339 (2018) 224–236

[4] G. Bae, Y. Xiong, S. Kumar, K. Kang, C. Lee, General aspects of interface bonding in kinetic sprayed coatings, Acta Mater. 56 (2008) 4858–4868

[5] H. Assadi, F. Gärtner, T. Stoltenhoff, H. Kreye, Bonding mechanism in cold gas spraying, Acta Mater. 51 (2003) 4379–4394

[6] M. Grujicic, C.L. Zhao, W.S. DeRosset, D. Helfritch, Adiabatic shear instability based mechanism for particle/substrate bonding in the cold-gas dynamic-spray process, Mater. Des. 25 (2004) 681–688.

[7] M. Hassani-Gangaraj, D. Veysset, V.K. Champagne, K.A. Nelson, C.A. Schuh, Adiabatic shear instability is not necessary for adhesion in cold spray, Acta Mater. 158 (2018) 430-439

[8] P.C. King, S. H. Zahiri, M. Jahedi, Microstructural refinement within a cold-spray copper particle, Mater. Trans. A. 40A (2009) 2115–2123.

[9] S. Guetta, M.H. Berger, F. Borit, V. Guipont, M. Jeandin, M. Boustie, Y. Ichikawa, K. Sakaguchi, K.Ogawa, Influence of Particle Velocity on Adhesion of Cold-Sprayed Splats, J. Therm. Spray Technol. 18 (2009) 331–342

[10] S.W.Dean, J.K. Potter, R.A. Yetter, T.J. Eden, V. Champagne, M. Trexler, Energetic intermetallic materials formed by cold spray, Intermetallics 43 (2013) 121–130

[11] K.H. Ko, J.O. Choi, H. Lee, The interfacial restructuring to amorphous: A new adhesion mechanism of cold-sprayed coatings, Mater. Lett. 175 (2016) 13–15

[12] C.D. Reddy, Zhi-Qian Zhang, S. Msolli, Junyan Guo, N. Sridhar, Impact induced metallurgical and mechanical interlocking in metals, Comput. Mater. Sci. 192 (2021) 110363

[13] T.H. Van Steenkiste, J.R. Smith, R.E. Teets, Aluminum coatings via kinetic spray with relatively large powder particles, Surf. Coat. Technol. 154 (2002) 237–252.

[14] R.N. Raoelison, Ch. Verdy, H. Liao, Cold gas dynamic spray additive manufacturing today: Deposit possibilities, technological solutions and viable applications, Mater. Des. 113 (2017) 266-287

[15] Z. Liu, H. Wang, M. Haché, E. Irissou, Y. Zou, Formation of refined grains below 10 nm in size and nanoscale interlocking in the particle–particle interfacial regions of cold sprayed pure aluminum, Scripta Mater. 177 (2020) 96-100.

[16] D.-Y. Kim, J.-J. Park, J.-G. Lee, D. Kim, S.J. Tark, S. Ahn, J.H. Yun, J. Gwak, K.H. Yoon, S. Chandra, S.S. Yoon, Cold spray deposition of copper electrodes on silicon and glass substrates, J. Therm. Spray Technol. 22 (2013) 1092–1102.

[17] A. A. Tiamiyu, C. A. Schuh, Particle flattening during cold spray: Mechanistic regimes revealed by single particle impact tests, Surf. Coat. Technol. 403 (2020) 126386.

[18] H. Assadi, F. Gärtner, T. Klassen, H. Kreye, Comment on 'Adiabatic shear instability is not necessary for adhesion in cold spray', Scripta Mater. 162 (2019) 512–514

[19] J. Wu, H. Fang, S. Yoon, H. Kim, C. Lee, Measurement of particle velocity and characterization of deposition in aluminum alloy kinetic spraying process, Appl. Surf. Sci. 252 (2005) 1368–1377

[20] T. Schmidt, F. Gärtner, H. Assadi, H. Kreye, Development of a generalized parameter window for cold spray deposition, Acta Mater. 54 (2006) 729–742.

[21] M. Grujicic, J.R. Saylor, D.E. Beasley,W.S. DeRosset, D. Helfritch, Computational analysis of the interfacial bonding between feed-powder particles and the substrate in the cold-gas dynamic-spray process, Appl. Surf. Sci. 219 (2003) 211-227.

[22] M. Hassani-Gangaraj, D. Veysset, V.K. Champagne, K.A. Nelson, C.A. Schuh, Response to Comment on 'Adiabatic shear instability is not necessary for adhesion in cold spray', Acta Mater. 162 (2019) 515-519

[23] H. Gao, C. Liu, F.H. Song, Molecular dynamics simulation of the influence factors of particle depositing on surface during cold spray, Adv. Mater. Mater, 652-654 (2013) 1916.

[24] T. Malama, A. Hamweendo, I. Botef, Molecular dynamics simulation of Ti and Ni particles on Ti substrate in the cold gas dynamic spray (CGDS) process, Materials Science Forum 828-829 (2015) 453

[25] A. Joshi, S. James, Molecular dynamics simulation study on effect of process parameters on coatings during cold spray process, Procedia Manuf. 26 (2018) 190

[26] A. Joshi, S. James, Molecular dynamics simulation study of cold spray process, J. Manuf. Process. 33 (2018) 136

[27] C. Schoner, T. Poschel, Orientation-dependent properties of nanoparticle impact, Phys. Rev. E 98 (2018) 022902
[28] S. Rahmati, A. Zúñiga, B. Jodoin, R.G.A. Veiga, Deformation of copper particles upon impact: A molecular dynamics study of cold spray, Comput. Mater. Sci. 171 (2020) 109219.

[29] S. Suresh, S.-Woo Lee, M. Aindow, H.D. Brody, V.K. Champagne Jr & A.M. Dongare, Unraveling the Mesoscale Evolution of Microstructure during Supersonic Impact of Aluminum Powder Particles, Sci. Reports 8 (2018) 10075.

[30] S.T. Oyinbo, T-C. Jen, Molecular Dynamics Simulation of Dislocation Plasticity Mechanism of Nanoscale Ductile Materials in the Cold Gas Dynamic Spray Process, Coatings, 10 (2020) 1079.

[31] S. Plimpton, Fast Parallel Algorithms for Short-Range Molecular Dynamics, J. Comp. Phys. 117 (1995) 1-19.

[32] M.S. Daw, M.I. Baskes, Embedded-atom method: Derivation and application to impurities, surfaces, and other defects in metals, Phys. Rev. B. 29 (1984) 6443–6453

[33] S. M. Foiles, M.I. Baskes, M.S. Daw, Embedded-atom-method functions for the fcc metals Cu, Ag, Au, Ni, Pd, Pt, and their alloys, Phys. Rev. B. 33 (1986) 7983

[34] A. Stukowski, Visualization and analysis of atomistic simulation data with (OVITO)–the Open Visualization Tool, Model. Simul. Mater. Sci. Eng. 18 (2009) 15012.

[35] C. Li, W. Li, H. Liao, Examination of the critical velocity for deposition of particles in cold spraying, J. Therm. Spray Technol. 15 (2006) 212–222.

[36] S. Yin, X. Wang, X. Suo, H. Liao, Z. Guo, W. Li, Deposition behavior of thermally softened copper particles in cold spraying, Acta Mater. 61 (2013) 5105–5118

[37] T. Schmidt, H. Assadi, F. Gartner, H. Richter, T. Stoltenhoff, H. Kreye, and T. Klassen, From Particle Acceleration to Impact and Bonding in Cold Spraying, J. Therm. Spray Technol. 18 (2009) 794–808.

[38] M. Hassani-Gangaraj, D. Veysset, K.A. Nelson, C.A. Schuh, Melt-driven erosion in microparticle impact, Nat. Commun. 9 (2018) 5077

[39] M. Hassani-Gangaraj, D. Veysset, K.A. Nelson, C.A. Schuh, Melting Can Hinder Impact-Induced Adhesion, Phys. Rev. Lett. 119 (2017) 175701

[40] D. Karthik, K. U. Yazar, A. Bisht, S. Swaroop, C. Srivastava, S. Suwas, Gradient plastic strain accommodation and nanotwinning in multi-pass laser shock peened 321 steel Appl. Sur. Sci. 487, (2019) 426-432

[41] R. Chakrabarty, J. Song, A modified Johnson-Cook material model with strain gradient plasticity consideration for numerical simulation of cold spray process, Surf. Coat. Technol. 397 (2020) 125981

[42] Y. Xiong , K. Kang, G. Bae, S. Yoon, C. Lee, Dynamic amorphization and recrystallization of metals in kinetic spray process, Appl. Phys. Lett. 92 (2008) 194101

Table 1: Impact velocity-dependent bonding mechanism in different regimes. Dominant bonding mechanisms are highlighted in bold.

Impact Velocity (m/s)	Bonding Mechanism	Interface strength	Regime
200	**Grain boundary-like**	Weak	I
300	**Grain boundary-like** and Metallurgical	Weak	I
400	**Grain boundary-like** and **Metallurgical**	Medium	I
500	Grain boundary-like, **Metallurgical** and **Mechanical**	Good	II
600	Grain boundary-like, **Metallurgical and Mechanical**	Strong	III

Figure captions:

Fig. 1. Spherical particle before impact, and the typical impact-induced deformation for the particle and substrate. The system is periodic in x- and y- directions, the top (z-) direction is free of any constraints, and the bottom few layers are constrained to support the system. The particle diameter *D* of 200 Å and substrate size in x-, y- and z- directions are 8*D*, 8*D and 4D*, respectively, considered for this work.

Fig. 2. (a) The change of equilibrium crater depth and equilibrium flattening parameter with impact velocity. In regime I, both crater depth and flattening (compression ratio) monotonically increase with velocity. Around the critical velocity (regime II), the crater depth and flattening ratio plateau with a small dip (attributable to scatter in the simulation results). At higher impact velocity (regime III), the carter depth sharply increases due to the larger melting of the substrate whereas the flattening ratio is almost flat and confined to the substrate crater. (b) The change in the crater depth and flattening ratio with time during the impact process is shown for the velocity of 500 m/s. Initially, the crater depth increases due to melting, and the plastically deformed substrate metal is pushed towards the interface edge by the penetrating particle. During elastic recovery of the substrate (after 20 ps), the crater depth partially reduces from its peak and then plateaus while the system is cooling. Similarly, the particle deforms continuously during the penetration period, sustains partial elastic recovery, and then plateaus to a constant value at a longer time.

Fig. 3. Snapshots of the temperature profile at 6ps for various impact velocities (from 300 m/s to 600 m/s). The total melt volume from both particle and substrate reaches a maximum of 6ps. All figures are on the same temperature scale of 300 K to 1400 K as shown in (b).

Fig. 4. (a) Evolution of the normalized number of atoms (N_m) exceeding the melt temperature of 1360K for the substrate and particle during the impact process. Empty and filled symbols represent the substrate and particle, respectively. (b) The normalized total number of atoms ($\sum N_m$) exceeds the melt temperature at each velocity. N_m and $\sum N_m$ are normalized to the total number of particle atoms.

Fig. 5. At 200 m/s & 300 m/s impact velocity, the interface is an amorphous structure mostly. This interface is a relatively weaker form of metallurgical bonding than the crystalline metallurgical bonding forming at higher impact velocities. At 300 m/s, small edge metallurgical grains are formed from interface sheared material at the one edge of the interface.

Fig. 6. At 400 m/s velocity of impact, the interface mostly shows an amorphous structure. At the edges of the interface, edge metallurgical bonding grains (EMG) are formed. The interface passing through these grains shows the onset of metallurgical bonding at this velocity. At impact velocities of 500 m/s and 600 m/s, the interface is mostly comprised of metallurgically bonded grains. The middle metallurgical (compressive region) grain is seamlessly connected to the substrate. Grain refinement near the interface is also observed. At 600 m/s impact velocity, the material jet creates a thin wide strip on top of the shear grains (also refer to Fig S3 for a cross-sectional view of the particle) and enhances the mechanical interlocking effect. The regions marked with orange and blue loops on the interface indicate the grain boundary-like (amorphous) and mechanical interlocking, respectively, and the rest (unmarked) of the interface region indicate the metallurgical bonding.

Fig. 7. Bottom view of the particle (along with the interface) at 500 m/s and 600 m/s impact velocities. White and green atoms indicate the grain boundary-like and metallurgical bonding, respectively. At 500 m/s, jetting of material around the particle (outside of the black circle) initiated, and metallurgical grains with stacking faults area visible at that boundary. At 600 m/s,

a wider jet of material around the particle enhances mechanical interlocking along with metallurgical bonding. The single-particle impact experiments (bottom panel) show jetting initiated at around the critical velocity, and also shows the wider jetting area as impact velocity increases [17], which are in good agreement with the current simulation results (top panel). (reprint permission is pending from Elsevier [ref. 17])

Fig. 8. The coverage of the interface with grain boundary-like interlocking, metallurgical bonded, and mechanical interlocking as a function of impact velocity. The Y-axis values are normalized with the interface surface area corresponding to impact velocity of 650 m/s. The interface surface area at the impact velocity of 650 m/s is almost 3 times that of interface surface area at 300 m/s. Three distinct regimes are identified based on the trend of surface area coverage by the dominant interlocking mechanism and this matches with the three regimes in the crater depth and flattening parameter pattern characteristics shown in Fig. 2(a).

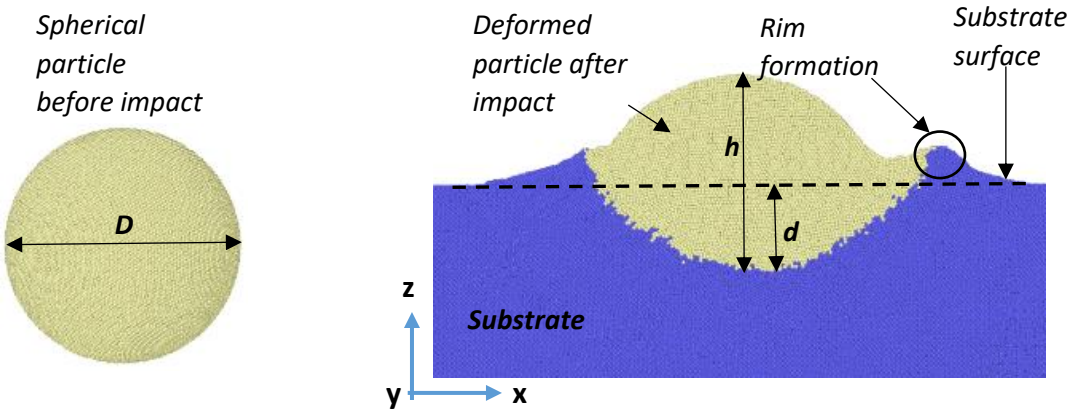
Spherical particle before impact
D
Deformed particle after impact
Rim formation
Substrate surface
h
d
Substrate
z
y
x

Fig. 1

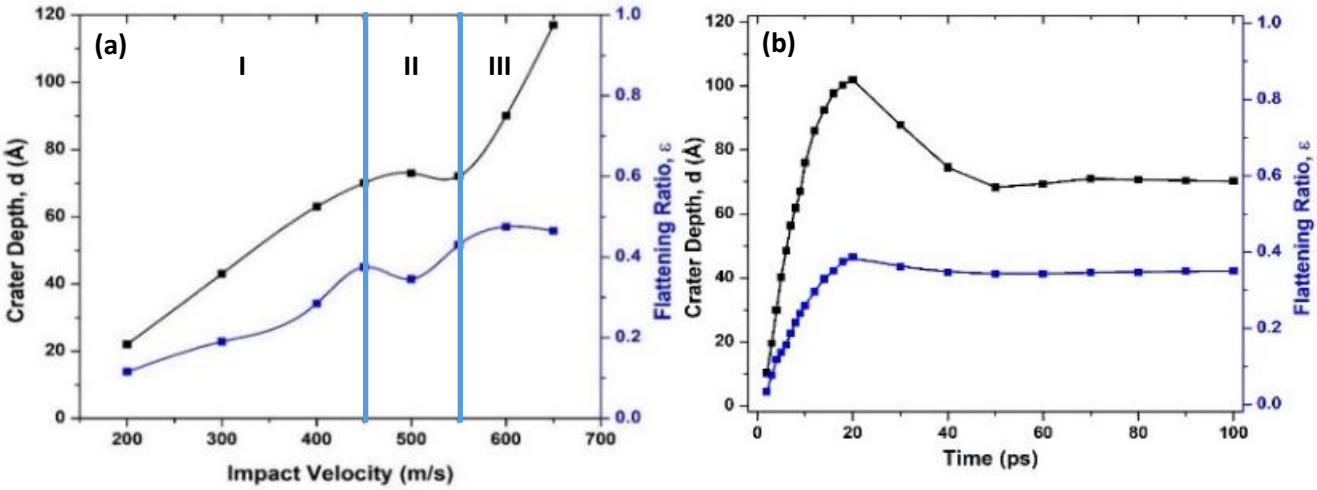
(a)
I
II
III
Crater Depth, d (Å)
Flattening Ratio, ε
Impact Velocity (m/s)
(b)
Crater Depth, d (Å)
Flattening Ratio, ε
Time (ps)

Fig. 2

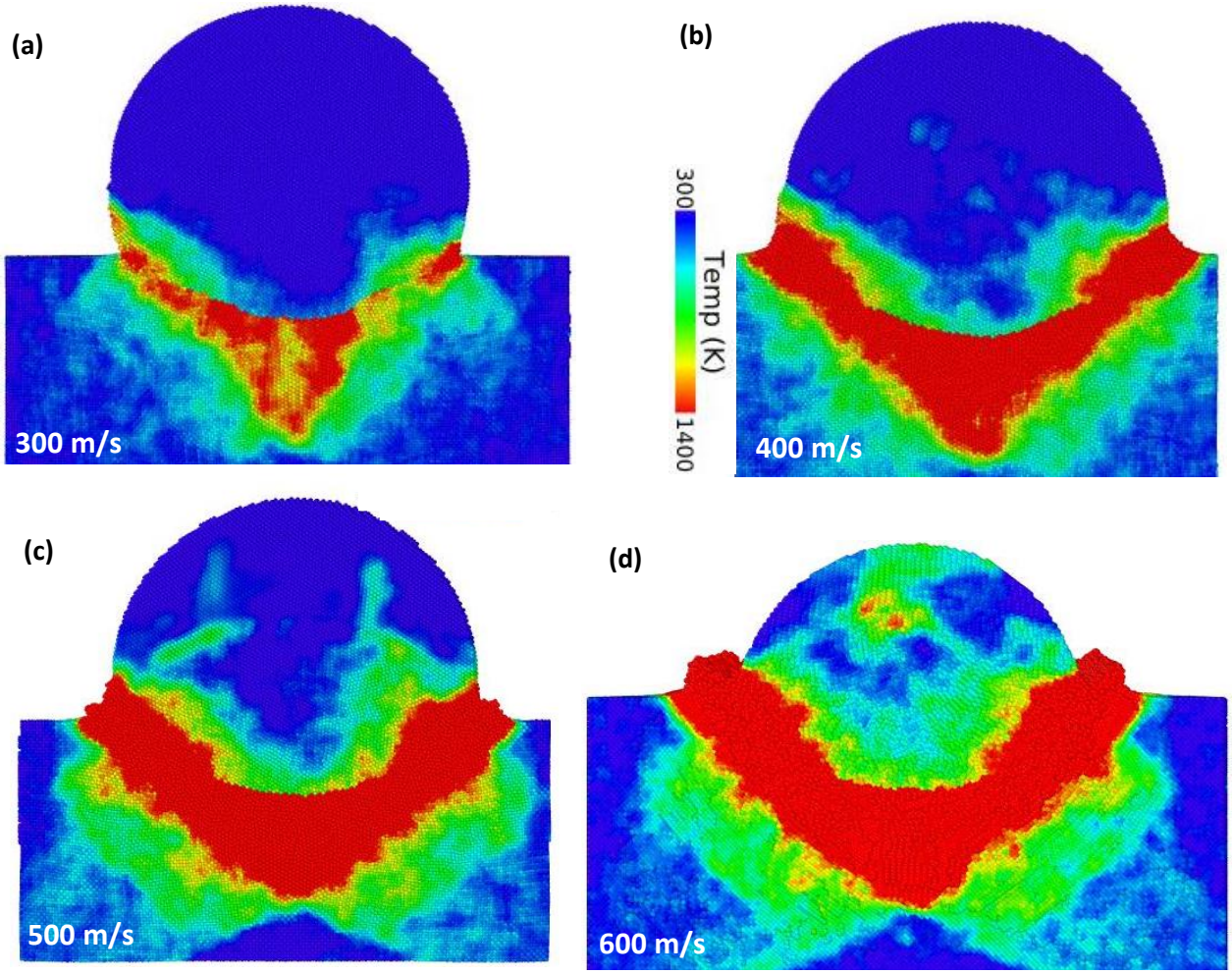

Fig. 3

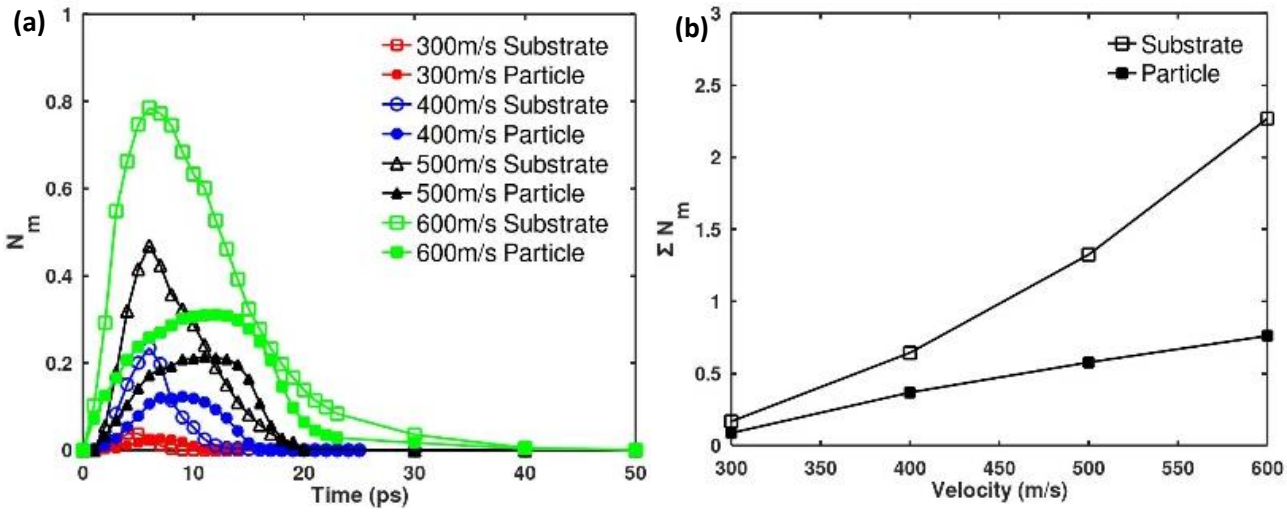
(a)
300m/s Substrate
300m/s Particle
400m/s Substrate
400m/s Particle
500m/s Substrate
500m/s Particle
600m/s Substrate
600m/s Particle
N m
Time (ps)
(b)
Substrate
Particle
Σ N m
Velocity (m/s)

Fig. 4

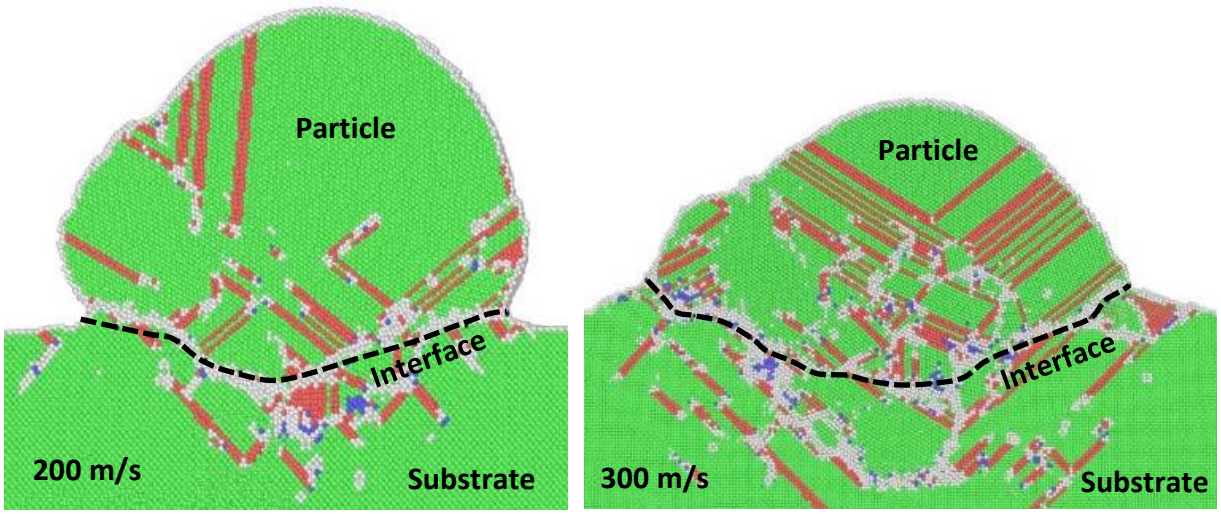
Particle
Interface
200 m/s
Substrate
Particle
Interface
300 m/s
Substrate

Fig. 5

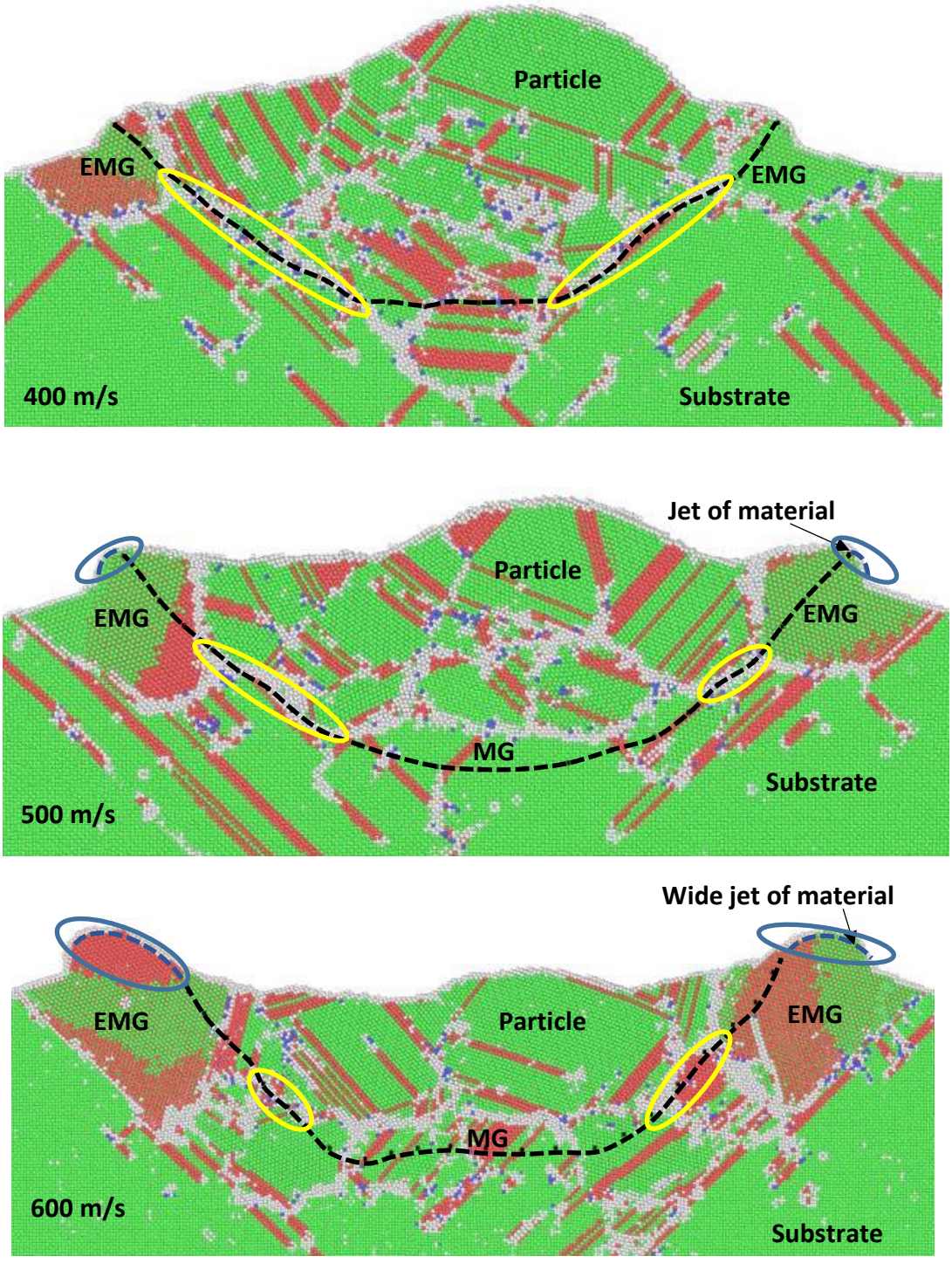
Particle
EMG
EMG
400 m/s
Substrate
Jet of material
Particle
EMG
EMG
MG
Substrate
500 m/s
Wide jet of material
EMG
Particle
EMG
MG
600 m/s
Substrate

Fig. 6

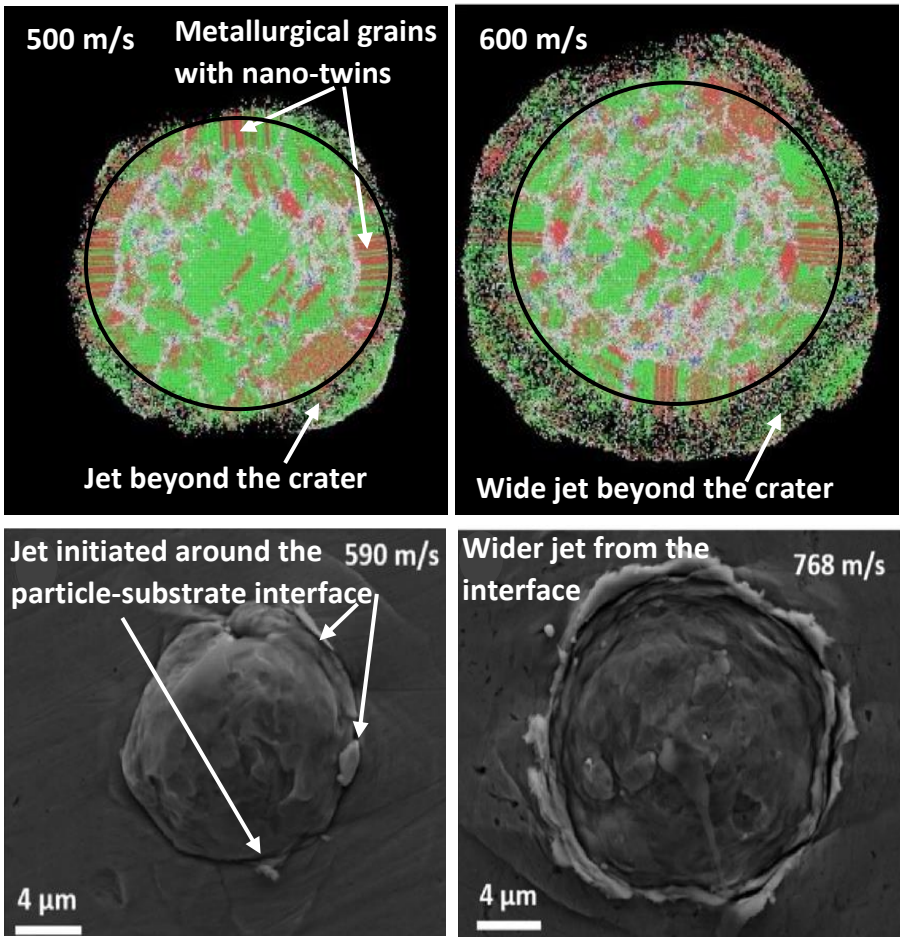
500 m/s
Metallurgical grains with nano-twins
Jet beyond the crater
600 m/s
Wide jet beyond the crater
Jet initiated around the particle-substrate interface
590 m/s
4 µm
Wider jet from the interface
768 m/s
4 µm

Fig. 7

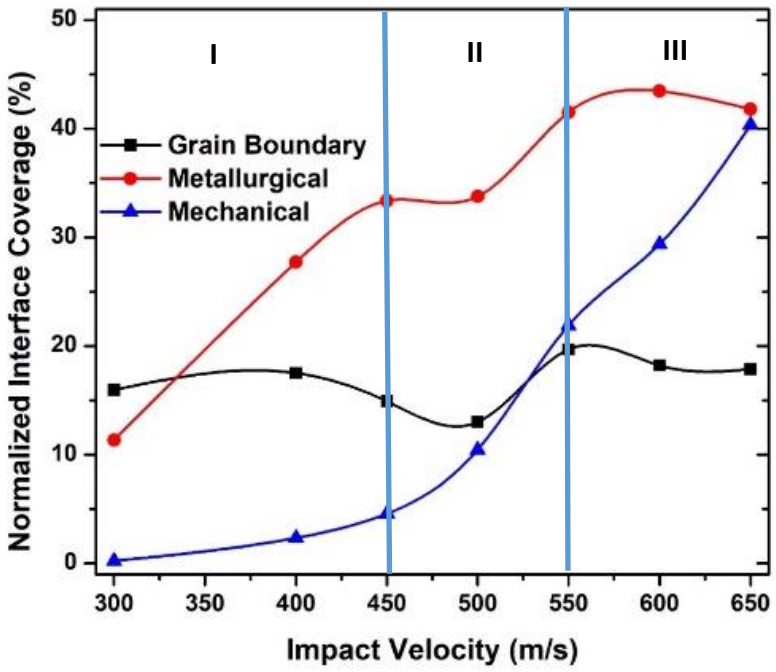
I
II
III
Grain Boundary
Metallurgical
Mechanical
Normalized Interface Coverage (%)
Impact Velocity (m/s)
0
10
20
30
40
50
300
350
400
450
500
550
600
650

Fig.8